Volume 10
Number 36
28 September 2022
Pages 12895–13272

Journal of Materials Chemistry C

Materials for optical, magnetic and electronic devices

rsc.li/materials-c

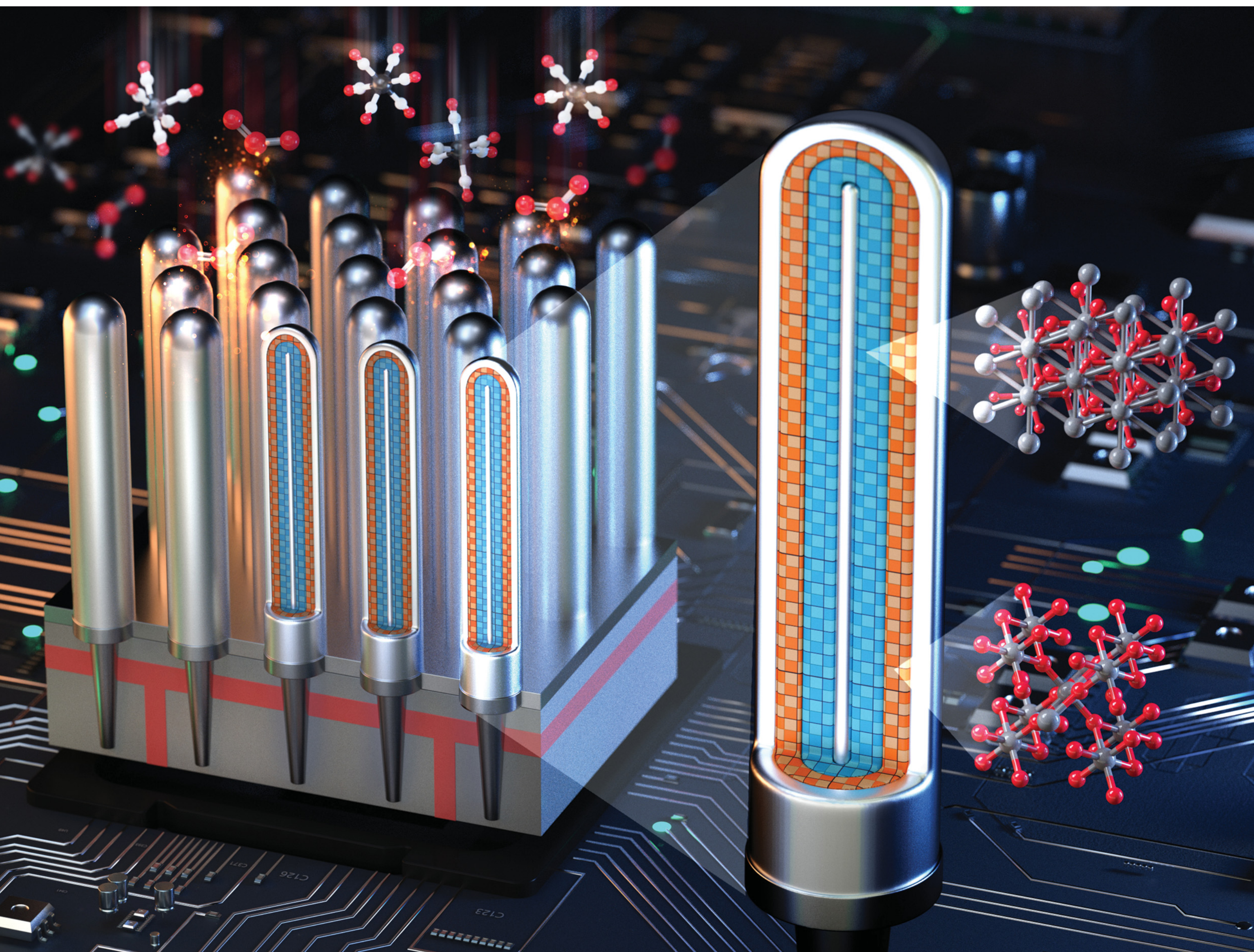

ISSN 2050-7526

ROYAL SOCIETY OF CHEMISTRY

PAPER

Woojin Jeon *et al.*

Reliable high work-function molybdenum dioxide synthesis *via* template-effect-utilizing atomic layer deposition for next-generation electrode applications

Journal of
Materials Chemistry C

ROYAL SOCIETY
OF CHEMISTRY

PAPER

View Article Online
View Journal | View Issue

Cite this: *J. Mater. Chem. C*, 2022, **10**, 12957

Reliable high work-function molybdenum dioxide synthesis *via* template-effect-utilizing atomic layer deposition for next-generation electrode applications†

Ye Won Kim,[a] Ae Jin Lee,[a] Dong Hee Han,[a] Dae Cheol Lee,[a] Ji Hyeon Hwang,[a] Youngjin Kim,[a] Songyi Moon,[b] Taewon Youn,[b] Minyung Lee[b] and Woojin Jeon *[a]

Published on 08 August 2022. Downloaded on 9/30/2022 7:42:00 AM.

Received 22nd May 2022,
Accepted 7th August 2022

DOI: 10.1039/d2tc02104h

rsc.li/materials-c

MoO_2, a conductive metal oxide, has attracted considerable attention as an electrode material in metal–insulator–metal (MIM) capacitors owing to its crystallinity and high work function. However, because MoO_2 is a metastable phase, it is difficult to deposit it using a chemical reaction-based thin film deposition method, which limits its practical device application. In this work, we developed an atomic layer deposition (ALD) process for MoO_2 thin films exhibiting high crystallinity and a very high work function of 5.5 eV. A mechanism in which the metastable MoO_2 phase is stabilized and crystallized was revealed based on the "template effect" by the interfacial layer formed on a substrate surface during the deposition process. Furthermore, the template effect governed not only the crystallinity but also the stoichiometry of the deposited thin film. By employing MoO_2, a rutile TiO_2 thin film exhibiting a dielectric constant as high as 150 was obtained, which is the highest value ever reported. The high work function was also attributed to leakage current suppression in the MIM capacitor. Therefore, the proposed MoO_2 ALD is applicable to developing next-generation dynamic-random-access-memory devices.

Introduction

Dynamic random-access memory (DRAM) is one of the most important semiconductor memories for application to various electronic devices. As semiconductor memories, capacitors are the most important components governing all DRAM operation characteristics. As DRAM capacitors, metal–insulator–metal (MIM) capacitors must exhibit sufficiently high capacitance densities and sufficiently low leakage currents to ensure robust device operation. To date, most research conducted to achieve these objectives has been focused on developing high-dielectric-constant (high-*k*) materials.[1,2] However, because these two requirements are trade-offs, no high-*k* material has been developed yet that can satisfy the requirements for application to next-generation DRAM devices. In contrast, although the electrode properties also strongly influence those of the MIM capacitor,[1,3–5] research on electrode deposition to develop MIM capacitor materials has been limited.

To enhance the electrical properties of MIM capacitors, the electrode must exhibit both a high work function and insulator–coherent crystallinity. Because most current conduction mechanisms are related to the barrier height between the insulator and electrode,[6] a higher work function is favorable for increasing the barrier height.[7] Furthermore, the crystal structural coherency between the insulator and electrode strongly influences the insulator crystallinity and, in turn, governs the insulator dielectric constant.[8–11] For decades, TiN has been employed as a DRAM capacitor electrode because the crystallinity of TiN is coherent with ZrO_2[4,12] and it has a facile deposition process.[13,14] However, TiN exhibits a relatively low work function (4.2 eV)[15] and inadequate crystallinity when combined with higher-*k* dielectrics such as TiO_2 and $SrTiO_3$,[16,17] limiting its application to next-generation DRAM devices.

MoO_2 has been proposed as a candidate suitable for application to various electrode materials. For instance, a relatively high dielectric constant of 70 was achieved by combining MoO_2 with rutile TiO_2 because their crystal structures were coherent.[18] Moreover, MoO_2 exhibits high thermal stability, which makes MoO_2 a promising electrode material for application to MIM capacitors. However, because MoO_2 is a metastable phase, an appropriate deposition process for adapting practical electronic devices has not been proposed yet. The previous

[a] *Department of Advanced Materials Engineering for Information and Electronics, and Integrated Education Program for Frontier Science & Technology (BK21 Four), Kyung Hee University, Yongin, Gyeonggi 17104, Korea. E-mail: woojin.jeon@khu.ac.kr*

[b] *SK Hynix, Inc., Icheon, Gyeonggi 17336, Korea*

† Electronic supplementary information (ESI) available. See DOI: https://doi.org/10.1039/d2tc02104h

Published on 08 August 2022. Downloaded on 9/30/2022 7:42:00 AM.

results about MoO_2 formation employed pulsed laser deposition[18] or additional reduction processes,[19] which were not applicable to the actual electronic device manufacturing process. Most of the deposition processes, such as chemical vapor deposition and atomic layer deposition (ALD), based on the oxidation reaction only achieved MoO_3 thin film, which is an insulator.[20,21] In this regard, MoO_2 thin films cannot be prepared using ALD methods even though ALD is the key to applying MoO_2 thin films to DRAM capacitors, resulting in the utilization of MoO_2 for actual electronic devices being limited.

Therefore, we developed an ALD method to deposit metastable MoO_2 thin films onto substrates and investigated the electrical properties of the deposited films for application to DRAM capacitor electrodes. Thin films grown using ALD exhibit substrate–coherent crystal structures, which is called the "template effect." To develop the ALD method, the template effect was adopted using TiN substrates to grow MoO_2 thin films exhibiting designated crystal structures and to investigate the template-effect-induced MoO_2 formation mechanism and the MoO_2 microstructure. Furthermore, MoO_2 thin-film properties were evaluated to apply MoO_2 to MIM capacitor electrodes. Owing to both the MoO_2 thin-film crystallinity and high work function, the MIM capacitor electrical properties were enhanced.

Experimental procedure

Thin film deposition process conditions

MoO_x ($2 \leq x \leq 3$) thin film was deposited by means of ALD (iOV dX1, iSAC research) using molybdenum hexacarbonyl ($Mo(CO)_6$) as the Mo precursor. The deposition process of MoO_x was performed at 170 °C. The substrate consisted of 50 nm-thick TiN (deposited by chemical vapor deposition process) as a bottom electrode on a thermally oxidized (100) Si wafer. Ozone (O_3, 200 g m^{-3}) and H_2O were employed as reactants. The deposited MoO_x thin film was annealed at 600 °C for 30 s in N_2 by a rapid thermal annealing (RTA) system (MIRA-5050, ULVAC). The TiO_2 ALD deposition process was performed using pentamethyl cyclopentadienyl Ti trimethoxide ($Ti(Me_5Cp)(OMe)_3$, Star-Ti) and O_3 as the Ti precursor and reactant, respectively. In addition, Al_2O_3 for the Al-doped TiO_2 (ATO) thin film was deposited with trimethylaluminium ($Al(CH_3)_3$, TMA) and O_3 as the Al precursor and reactant, respectively, with a fixed sub-cycle ratio of 1 : 90. The deposition temperature for TiO_2 and Al_2O_3 was set to 320 °C.

MIM capacitor structure fabrication process

To measure the MIM capacitor electrical properties, 20 nm-thick RuO_2 and 50 nm-thick Pt films were sequentially deposited using radio frequency (rf)- and direct current (dc)-sputtering (KVS-2000L, Korea Vacuum Tech), respectively, through a metal shadow mask with a ∅300 μm hole to serve as the top electrode, and the electrode was subsequently annealed at 400 °C for 30 s in an N_2/O_2 mixture by the RTA system. A schematic of the fabricated MIM structure is depicted in Fig. S1 in the ESI.†

Structure, chemical state, and electrical property analyses

The film thickness was determined by calculating the layer density, which was measured using X-ray fluorescence spectroscopy (ARL Quant'X, Thermo Scientific™) and was correlated with spectroscopic ellipsometry (ESM-300, J. A. Woollam) measurements and transmission electron microscopy (TEM, JEM-2100F) images. The chemical state of the dielectric was investigated *via* X-ray photoelectron spectroscopy (XPS, K-Alpha+, ThermoFisher Scientific™). Glancing angle incident X-ray diffraction (GA-XRD, X'pert Pro, PANalytical) was used at 0.5° incident angle to examine the film crystal structures. The MIM capacitor electrical properties were evaluated by measuring the capacitance *versus* voltage and current *versus* voltage characteristics using Agilent 4284 and 4155C meters, respectively. The TiO_2/MoO_2 crystal structural coherency was analysed *via* high-resolution transmission electron microscopy (HR-TEM). Ultraviolet photoelectron spectroscopy was performed to measure the MoO_2 work function.

Results and discussion

Development of ALD for depositing MoO_2 thin films

MoO_2 ALD was investigated using $Mo(CO)_6$ as a Mo precursor at 170 °C to avoid the thermal decomposition of $Mo(CO)_6$, which occurred at 180 °C (Fig. S2, ESI†). TiN and SiO_2 substrates were used, which represented the TiN bottom electrode and oxide mold during the actual DRAM fabrication process, to demonstrate the applicability of the MoO_x thin film for the bottom electrode of the DRAM capacitor. H_2O and O_3 were employed as the O sources (reactants) to determine how the chemistry of the deposited film affected the oxidation potential difference. When either H_2O or O_3 was employed as the oxygen source, the precursor feeding time exhibited typical saturation behavior (Fig. S3a, ESI†). However, the deposition behavior was different depending on the reactant. For the same substrate, the precursor feeding saturation time was longer when O_3 was utilized rather than H_2O because the reactant governed the surface termination, thereby affecting the precursor adsorption chemistry.[22,23] Moreover, the cycle-dependent film thickness curves (Fig. S3c, ESI†) exhibited different numbers of incubation cycles. When O_3 was used, approximately 100 incubation cycles were required, in contrast to almost no incubation cycles when H_2O was used. These results suggest that the Mo precursor was chemisorbed slower on the O_3-terminated surface than on the H_2O-terminated one. Indeed, the film growth per cycle (GPC) was almost identical at 0.025 nm per cycle for the depositions using H_2O on SiO_2, H_2O on TiN, and O_3 on SiO_2 substrates, indicating that the reactant only affected the Mo precursor chemisorption on the substrate surface, not the chemical reaction with the Mo precursor. However, the film GPC increased to 0.035 nm per cycle when O_3 was used on the TiN substrate. Since the saturation feeding times and number of incubation cycles were identical when O_3 was used on both the TiN and SiO_2 substrates, the film GPC difference originated from the chemical reaction between the Mo precursor and O_3 on the TiN substrate, not from the surface termination.

 This journal is © The Royal Society of Chemistry 2022

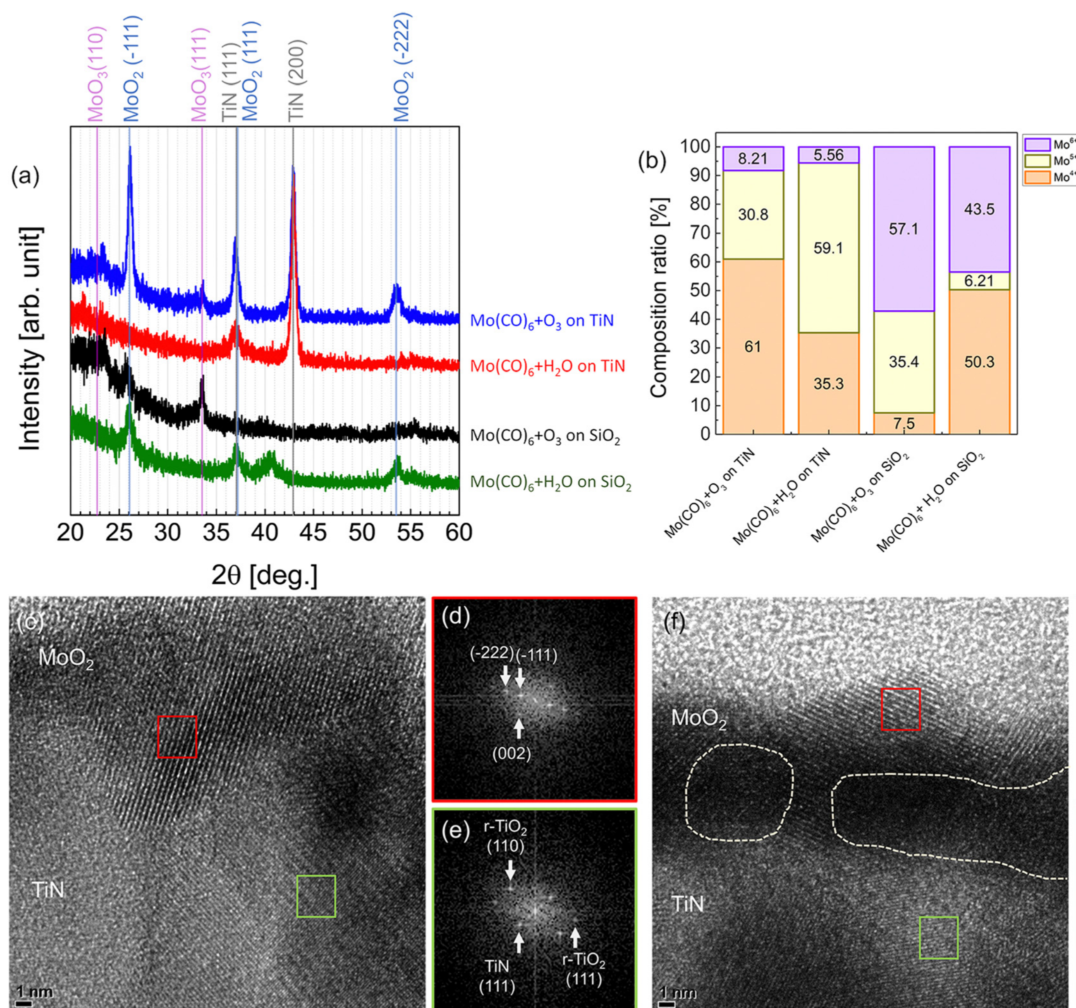

Fig. 1 (a) XRD patterns and (b) composition ratio of oxidation states of MoO_x thin films deposited under various conditions. (c) HR-TEM image of TiN/MoO_x deposited using O_3 and FFT patterns of (d) MoO_2 (indicated by red box in (c)) and (e) TiN surface (indicated by green box in (c)). (-111), (111), and (-222) in (d) indicate the planes of monoclinic phase MoO_2. r-TiO_2 and a-TiO_2 in (e) indicate rutile- and anatase-phased TiO_2, respectively. (f) HR-TEM image of TiN/MoO_x deposited using H_2O. The dashed line region indicates an amorphous area in the film. FFT patterns of (g) MoO_2 (indicated by red box in (f)) and (h) the TiN surface (indicated by the green box in (f)).

The crystal structures of the thin films deposited using H_2O and O_3 were also considerably different depending on the process conditions, as confirmed using XRD (Fig. 1a). For the films deposited on the SiO_2 substrate, the XRD pattern exhibited diffraction peaks corresponding to less-oxidized MoO_2 when H_2O was employed as the reactant. Meanwhile, the film deposited using O_3 on the SiO_2 substrate exhibited the MoO_3 crystal structure. This different oxidation state is attributed to the different H_2O and O_3 oxidation potentials. However, the oxidation state of the films deposited on the TiN substrate was not determined by the reactant oxidation potential. The XRD pattern for the film deposited using H_2O on the TiN substrate did not exhibit any diffraction peaks originating from MoO_2 or MoO_3. Moreover, the XRD pattern for the film deposited using O_3 on the TiN substrate exhibited very strong diffraction peaks at 26.1 and 53.8°, corresponding to the (-111) and (-222) planes of the monoclinic MoO_2 crystal structure, respectively. Although the Mo oxidation state is 6+ in $Mo(CO)_6$ and O_3 exhibits stronger oxidation potential than H_2O, Mo^{4+} was obtained when O_3 was used as the oxygen source on the TiN substrate. Therefore, XPS was used to reveal the Mo oxidation states in the thin films. Mo 3d peaks are composed of Mo $3d_{5/2}$ peaks centered at the 229.4, 231.3, and 233.1 eV binding energies (BEs), which correspond to Mo^{4+}, Mo^{5+}, and Mo^{6+}, respectively.[24,25] The deconvoluted Mo 3d XPS spectra revealed that all the deposited molybdenum oxide (MoO_x, where $2 \leq x \leq 3$) thin films exhibited Mo in different oxidation states (Mo^{4+}, Mo^{5+}, and Mo^{6+}) in various compositional ratios (Fig. 1b and Fig. S4, ESI†). For MoO_x thin films deposited on SiO_2 substrates, the composition of Mo in different oxidation states followed the same trend observed in the corresponding XRD spectra. Namely, the film deposited using O_3 exhibited a higher Mo^{6+} content (87.0 at%) than the counterpart film deposited using H_2O (0.9 at%). For MoO_x thin films deposited on TiN substrates, however, the Mo^{4+}, Mo^{5+} and Mo^{6+} contents were exactly opposite to the oxidation potential. The Mo^{6+}

Published on 08 August 2022. Downloaded on 9/30/2022 7:42:00 AM.

Published on 08 August 2022. Downloaded on 9/30/2022 7:42:00 AM.

contents were increased from 8.21 to 17.2% even when the oxidation potential of oxidant was decreased from O_3 to H_2O, respectively. Thus, when H_2O was used as the reactant, Mo^{5+} was dominant in the film (67.1 at%). Moreover, the film deposited using O_3 on the TiN substrate exhibited the highest Mo^{4+} content (61.0 at%). In other words, among the examined conditions, ALD using O_3 on the TiN substrate was the most facile for forming metastable MoO_2, which contains the most reduced oxidation state of Mo among the different states, even though the process employed a higher-oxidation-potential reactant on a substrate vulnerable to oxidation.

Furthermore, when MoO_x films were deposited using H_2O on the TiN substrate, the film Mo^{4+} content was not negligible (15.7 at%), indicating that although these process conditions also induced MoO_2 formation, the MoO_2 did not crystallize in these MoO_x thin films. Moreover, although the film deposited using O_3 on the TiN substrate contained 8.21 at% MoO_3, the MoO_3 did not crystallize. Because only the MoO_x thin film deposited using O_3 on the TiN substrate exhibited both crystallized MoO_2 and amorphous MoO_3, the TiN surface may have predominantly contributed to the film crystal structural formation. To clarify the origin of the MoO_2 formation and crystallization, TiN/MoO_x thin-film surfaces were investigated using TEM. Fig. 1c–e show the TEM images of the MoO_x thin film deposited using O_3 on the TiN substrate. As determined from the lattice fringes, the MoO_x layer exhibited a highly crystallized structure, as corroborated by the corresponding XRD spectra. Moreover, all the diffraction points in the fast-Fourier-transform (FFT) pattern (Fig. 1d) corresponded only to the MoO_2(-111), (111), and (-222) planes, and the FFT pattern did not exhibit any diffraction points corresponding to MoO_3 planes. This result indicated that the MoO_x film deposited using O_3 on the TiN substrate exhibited remarkably high-crystallinity monoclinic MoO_2, as confirmed by the corresponding XRD patterns. To clarify the origin of the exceptional MoO_x crystallization to MoO_2, the TiN–MoO_2 interface was observed (Fig. 1e). As shown in Fig. 1c, the TiN layer also exhibited high crystallinity and a cubic structure. However, the interface between the TiN and MoO_2 layers clearly exhibited a coherence-free fringe pattern, indicating that MoO_2 did not epitaxially grow from the TiN substrate. Because the TiN crystal structure exhibited a lattice constant quite different from MoO_2, TiN did not contribute to MoO_2 crystallization. However, the fact that the MoO_x deposited with only O_3 reactant on the TiN substrate exhibited strong crystallization to MoO_2 indicates the presence of a driving force that induced the formation of MoO_2 and crystallization. Meanwhile, the FFT pattern exhibited points originating from not only TiN but also rutile TiO_2 (Fig. 1e), indicating that O_3 probably induced rutile TiO_2 crystal formation at the TiN–MoO_x interface during MoO_x deposition. Rutile TiO_2 exhibits a lattice constant quite like that of MoO_2 and a very small lattice mismatch of less than 5%.[18] Fig. 1f–h shows a micro-structure of the TiN and MoO_x interface deposited using H_2O. In contrast to the MoO_x deposited using O_3, a slight fringe in MoO_x was observed in a limited region and an amorphous region was clearly observed (dashed line region in Fig. 1f), indicating a low crystallinity of MoO_x thin film using H_2O. This can be confirmed from the absence of a diffraction peak in the XRD pattern.

Crystallized MoO_2 formation mechanism by the template effect

The transition metal oxides have various types of crystal structures. In most cases, the phase stability is influenced by the Gibbs free energy difference for each phase. For example, TiO_2 has a rutile phase at high temperature or in the bulk state because the rutile phase is more stable than the anatase phase, according to the Gibbs free energy. However, in the case of the film getting thinner, the ratio of surface is unavoidably large, and the phase is determined by the size of individual grains. Indeed, the results of TiO_2 thin film deposition indicated the formation of anatase-phase TiO_2 even though the Gibbs free energy is higher for the anatase phase than that of the rutile phase. This factor, known as the surface energy effect, governs the stabilized phase in the thin film, and can be described by basic thermodynamic considerations. In the case of the film having two different crystal structures, one phase exhibits lower surface energy and the other exhibits lower bulk energy; consequently the bulk-to-surface content ratio will govern the thin film crystal structure.[26,27] With increasing film thickness, the bulk volume increases, thereby crystallizing the structure exhibiting the crystal structure of lower bulk energy. At the early stage of thin film deposition, the surface ratio is dominant; hence, the crystal structure of the deposited thin film tends to have a crystal structure coherent with that of the substrate to minimize the surface energy, which is called the "template effect". To confirm that the crystallized MoO_2 thin film had epitaxially grown *via* the "template effect", the film-thickness-dependent crystallinity of the MoO_x thin films deposited using O_3 on the TiN substrate was investigated using both XRD and XPS (Fig. 2 and Fig. S5, ESI†). In Fig. 2a, the XRD patterns of the thin films having thicknesses up to 7.5 nm only exhibited peaks originating from MoO_2. In contrast, a peak at 33.4°, corresponding to the MoO_3(111) plane, was observed in the XRD pattern of the 10 nm-thick thin film. The film thickness also affected the oxidation state of the deposited MoO_x thin film. Fig. 2b shows the film-thickness-dependent Mo^{4+}, Mo^{5+}, and Mo^{6+} contents of the thin films, as obtained from the deconvoluted Mo 3*d* XPS spectra of the MoO_x thin films deposited at various thicknesses using O_3 on the TiN substrate (Fig. 2b and Fig. S5, ESI†). In the 1 nm-thick MoO_x thin film, the Mo^{6+} content was markedly decreased to 9.9 at%. Simultaneously, the contents of Mo^{4+} and Mo^{5+} were significantly increased with a decrease in the thickness of the thin film from 4.5 to 3.5 nm. In the 4.5 to 10.0 nm-thick films, the Mo^{4+}, Mo^{5+}, and Mo^{6+} contents negligibly changed.

This change in oxidation state can be attributed to the difference between the oxide formation energies of TiO_2 and MoO_3. The oxide formation energy of TiO_2 is relatively low, inducing the oxygen scavenging effect, which corresponds to the oxidation of the TiN surface to TiO_2 or TiO_xN_{1-x} using the oxygen from the film deposited on the surface.[4] During the deposition of the MoO_x thin film, the MoO_x is reduced on the TiN surface owing

This journal is © The Royal Society of Chemistry 2022

Published on 08 August 2022. Downloaded on 9/30/2022 7:42:00 AM.

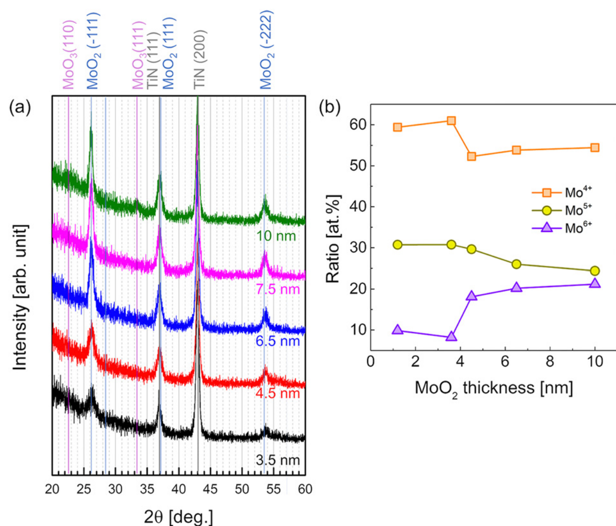

Fig. 2 (a) XRD patterns of MoO_2 thin films deposited at various thicknesses. (b) Mo^{4+}, Mo^{5+}, and Mo^{6+} ratios plotted as functions of MoO_2 film thickness.

to the oxygen scavenging effect of TiN. The XPS results indicate that the oxygen scavenging effect changed the thickness by approximately 3.5 nm, which is consistent with the oxygen scavenging effect on HfO_2 by La.[28] Moreover, this effect can explain the formation of TiO_2 on the TiN surface during the deposition of MoO_x using H_2O (Fig. 1h). The TiO_2 at the surface of TiN in MoO_x deposited using H_2O did not form due to the oxidation by H_2O, but by the oxygen scavenging effect of TiN owing to the oxygen present on the deposited MoO_x film. However, it should be noted that the formation of rutile TiO_2 on the surface of TiN was attributed to the use of O_3 reactant. The XRD result of the MoO_x deposited using H_2O on TiN indicates that the formation of rutile TiO_2 due to the oxygen scavenging effect was insufficient to induce the crystallization of MoO_2. This thickness dependency on the oxidation state indicates that the template effect had affected not only the crystallinity but also the oxidation state of the deposited film.

Moreover, the difference in crystallization behaviors of MoO_2 and MoO_3 in the MoO_x thin film should be considered. Although the MoO_3 composition was almost identical in the thin films with thicknesses above 4.5 nm, the formation of crystalline MoO_3 was observed only at the thickness of 10 nm. Notably, in the thermodynamic aspect, the crystallization in the thin film was observed above a fixed thickness where a sufficiently large nucleus can be formed. However, the crystallization of MoO_2 was opposite to this thermodynamic aspect. The thinner MoO_2 film could be crystallized easily, and an extremely strong diffraction pattern of MoO_2 was observed for a 3.5 nm-thick MoO_x film; this would not be possible without the presence of an external driving force for the crystallization. This driving force corresponds to the template effect on account of the rutile-phased TiO_2. The surface energy between the TiN and MoO_x interface could be reduced *via* crystallization to the monoclinic MoO_2, which has a crystallinity coherency with the rutile TiO_2. Although the Mo^{4+} content in the MoO_x thin film deposited using H_2O on TiN was also high, most part of the film remained in the amorphous phase (Fig. 1f). This was because enough rutile TiO_2 did not form at the surface of TiN with the H_2O reactant owing to its low oxidation potential. Although rutile TiO_2 was observed (Fig. 1h) probably due to the oxygen scavenging effect, the crystallization of MoO_2 was not observed owing to the poor crystallinity of the rutile TiO_2.

Based on these results, the following mechanism is proposed for MoO_2 crystallization during thin-film deposition (Fig. 3). During MoO_x ALD using O_3, the strong O_3 oxidation potential oxidizes the TiN surface to form rutile TiO_2. Moreover, the oxygen scavenging effect of TiN results in the reduction of the deposited MoO_x thin film to MoO_2. Owing to rutile TiO_2 and MoO_2 crystal structural coherency, MoO_x is deposited mostly as Mo^{4+} and then crystallizes to monoclinic MoO_2. The substrate crystal-structure-induced epitaxial growth decreased with increasing film thickness, resulting in different film-thickness-dependent crystal structures. These results suggest that the template effect originating from rutile TiO_2 on the TiN substrate surface plays a key role in metastable MoO_2 formation and crystallization.

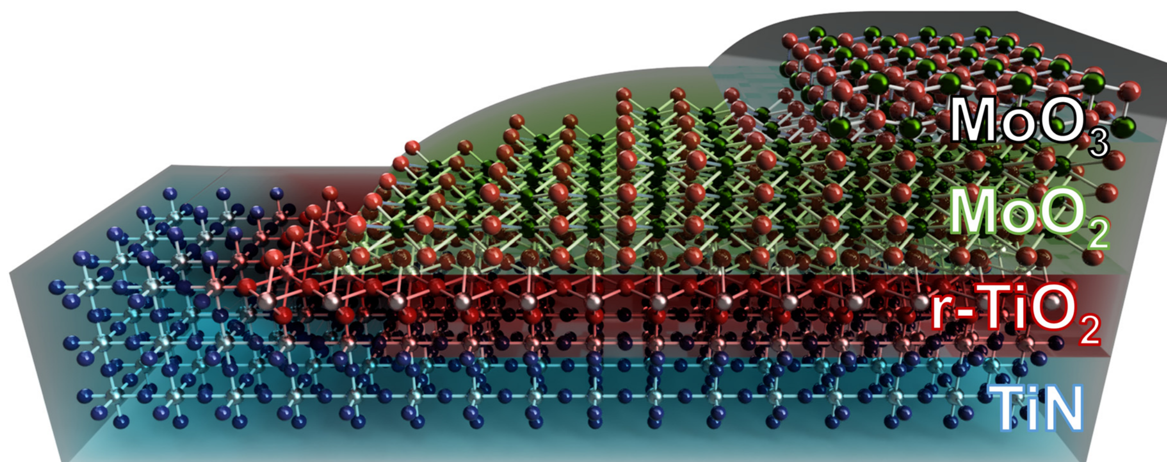

Fig. 3 Schematic diagram of the formation of MoO_2 and MoO_3 in MoO_x thin film depending on the film thickness.

Published on 08 August 2022. Downloaded on 9/30/2022 7:42:00 AM.

Evaluating electrical characteristics of MIM capacitors fabricated using MoO_2 electrodes

The template effect of the deposited MoO_2 thin-film electrode on *in situ* rutile TiO_2 formation was investigated for application to next-generation DRAM capacitors. The crystallinity of the TiO_2 thin film deposited on the MoO_2 thin film was investigated using XRD (Fig. 4a). Owing to the highly crystallized MoO_2 structure, the deposited TiO_2 film also exhibited high rutile crystallinity. In the XRD pattern, strong diffraction peaks corresponding to rutile TiO_2 were observed even though the TiO_2 film was only 18 nm thick. Furthermore, the corresponding TEM image (Fig. 4b) shows that the high rutile TiO_2 crystallinity solely originated from the MoO_2 thin-film crystallinity. Lattice fringe coherency clearly appeared at the TiO_2–MoO_2 interface. The FFT patterns obtained for the TiO_2 and MoO_2 layers (Fig. 4c and d, respectively) were almost identical. Then, the dielectric constants were evaluated for the TiO_2 thin film deposited on the MoO_2 and TiN films (Fig. 4e). The TiO_2 thin film bulk dielectric constant deposited on the MoO_2 extracted from the curve of the physical thickness (t_{phy}) *vs.* the equivalent oxide thickness (t_{ox}) was 150, which is the highest dielectric constant ever reported for deposited TiO_2 thin films,[29–32] whereas 48 for the TiO_2 thin film deposited on TiN. Moreover, the t_{phy}–t_{ox} curve exhibited an almost negligible *y*-intercept, implying that the TiO_2 thin film crystallinity was not degraded at the TiO_2–MoO_2 interface. These results suggest that the rutile TiO_2 crystallinity was attributed to MoO_2-crystal-structure-induced epitaxial growth.

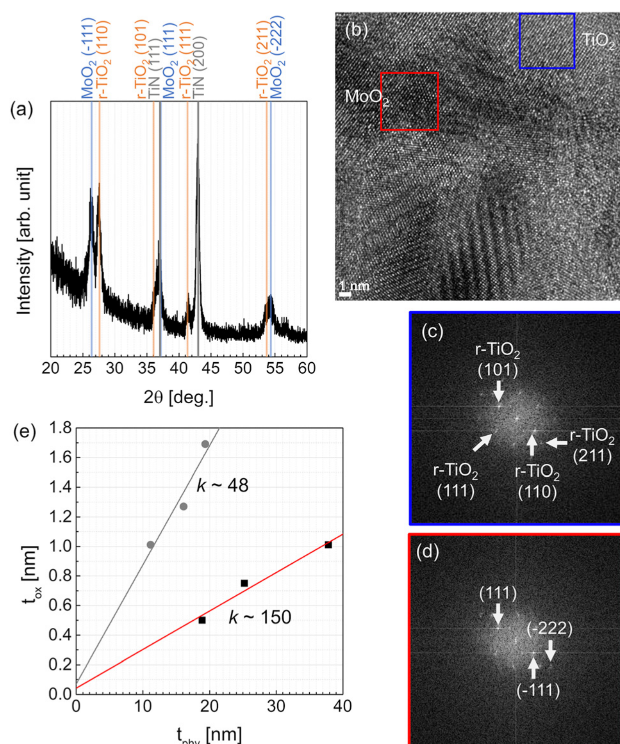

Fig. 4 (a) XRD pattern of 10 nm-thick TiO_2 thin film deposited on MoO_2. (b) HR-TEM image of TiO_2/MoO_2 and FFT patterns of (c) TiO_2 layer (indicated by blue box in (b)) and (d) MoO_2 layer (indicated by red box in (b)), and (e) t_{phy}–t_{ox} curve of TiO_2 deposited on MoO_2 (black square symbol and red line) and TiN (gray circle symbol and gray line).

Notably, the exceptional TiO_2 dielectric constant as high as 150 was achieved because the MoO_2 thin film deposited using the developed ALD method exhibited an excellent crystal structure. Even when an Ru or an RuO_2 substrate was employed to epitaxially grow TiO_2, the highest *k* achieved was 120.[32] Furthermore, the higher lattice mismatch between MoO_2 and rutile TiO_2 (4.6%) than that between RuO_2 and rutile TiO_2 (2.0%) indicated that the high dielectric constant of the TiO_2 thin film was ascribed to the exceptionally high crystallinity of the MoO_2 thin film deposited using O_3 on the TiN substrate.

The above results suggest that the MoO_2/TiN structure is the most promising capacitor electrode for further improving the electronic applications. However, for DRAM applications, the physical thickness of not only the insulator but also the electrode is strictly limited owing to extremely scaled pitch size in the three-dimensional structure of the capacitor (Fig. 5a). The minimum thickness of MoO_2 was evaluated to investigate the actual DRAM application capability of the MoO_2/TiN structure. As shown in Fig. 5b, the template effect for rutile-phased TiO_2 formation depending on the MoO_2 thickness was investigated. For the MoO_2 thicknesses of 3.1 (50 ALD cycles) and 4.8 nm (75 ALD cycles), the deposited TiO_2 thin films exhibited *k* values of 148.2 and 153.1, respectively, indicating that the TiO_2 was well crystallized to the rutile phase. In the case of 0.5 nm-thick MoO_2 (15 cycles), the TiO_2 thin film demonstrated a *k* value of 92.5, implying that MoO_2 with a thickness more than 0.5 nm, which corresponds to the minimum thickness to form the monolayer, can contribute to the formation of rutile-phased TiO_2. However, for thicknesses lower than 0.5 nm, the *k* value of TiO_2 dramatically decreased, reaching 58.0 for 0.14 nm-thick MoO_2 (5 cycles). Simultaneously, the leakage current density of the MIM structure was also evaluated. As observed in the dependence of the *k* value of TiO_2 on the MoO_2 thickness, the leakage current density also increased for MoO_2 thicknesses lower than 3 nm (50 cycles). This variation in leakage current density can be attributed to the difference between the work functions of TiN and MoO_2. The variation in the work function of the MoO_2/TiN structure with the MoO_2 thickness was also investigated (Fig. 5c). When the thickness of MoO_2 was more than 3 nm, the work function of the structure was 5.5 eV, which is a relatively high value among those of potential materials for electrode applications (Table 1 and Fig. 5d). With the decrease in the thickness of MoO_2 below 3 nm, the work function of the structure gradually decreased. This result indicated that the high work function of the structure can be attributed to the work function of MoO_2, and as the thickness of MoO_2 decreased, the work function of the structure was governed by the TiN.

Finally, MIM capacitors were fabricated using MoO_2 electrodes to determine the minimum t_{ox} at a leakage current density of 10^{-6} A/cm^2 at an applied bias of 0.8 V, which is called "t_{ox} scaling" (Fig. 6). The t_{ox} scaling was measured using an MoO_2 electrode instead of a TiN one in a TiO_2-based MIM capacitor. In the TiN electrode, the TiO_2 and Al-doped TiO_2 (ATO) thin film crystallized to anatase TiO_2 exhibiting a dielectric constant of 48 and 26.6, respectively, and resulting in the minimum t_{ox}

 This journal is © The Royal Society of Chemistry 2022

Published on 08 August 2022. Downloaded on 9/30/2022 7:42:00 AM.

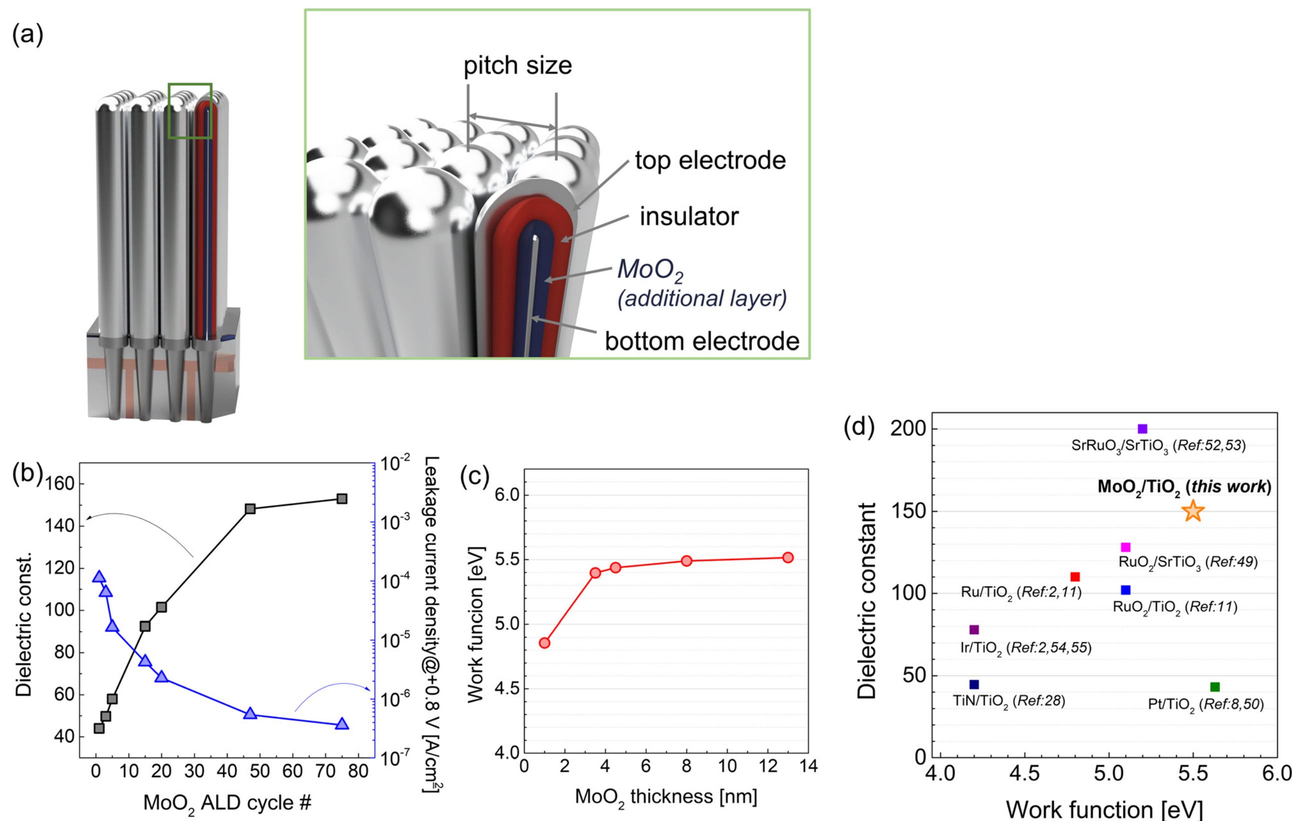

Fig. 5 (a) Schematic illustration of the DRAM capacitor. (b) *k* value and leakage current of the MIM capacitor consisting of (bottom) TiN/MoO_2/16 nm-thick and (top) TiO_2/RuO_2/Pt with varied MoO_2 thickness. (c) Work function of the TiN/MoO_2 structure depending on the MoO_2 thickness. (d) Work function of electrodes *vs.* dielectric constant of insulators deposited on the electrode plot for comparison of recent achievements about the electrode of MIM capacitors.

Table 1 Comparison of recent results about the electrode of MIM capacitors

Electrode material	Deposition technique (electrode)	Work function [eV]	Dielectric material	Deposition technique (dielectric)	Dielectric constant	Minimum t_{ox} [nm]
MoO_2 (this work)	ALD	5.5	TiO_2	ALD	150	0.44
MoO_2 (this work)	ALD	5.5	ATO	ALD	106	0.36
Ru[2,30]	CVD	4.8	TiO_2	ALD	110	0.8
Ru[2,33]	—	4.8	$SrTiO_3$	ALD	101	0.46
RuO_2[30]	CVD	5.1	TiO_2	ALD	102	0.56
RuO_2[34]	CVD	5.1	ATO	ALD	99.7	0.37
RuO_2[35]	—	5.1	$SrTiO_3$	ALD	128	0.43
Pt[36]	Sputter	5.63	TiO_2	ALD	43	2.44
TiN[15]	CVD	4.2	TiO_2	ALD	44.5	1.71
TiN[15]	CVD	4.2	ATO	ALD	44.54	1.69
$SrRuO_3$[37]	PLD	5.2	TiO_2	PLD	39	2.5
$SrRuO_3$[38]	Sputter	5.2	$SrTiO_3$	Sputter	200	0.4
Ir/IrO_2[2,39]	ALD	4.2	TiO_2	ALD	78	0.52

of 2.2 and 0.95 nm, respectively. In contrast, the TiO_2 and ATO thin film deposited on the MoO_2 film exhibited a dielectric constant of 150, and 106, respectively, leading to a t_{ox} of 0.7, and 0.357 nm, respectively, which is the best result ever reported.[2,34,40] Notably, both t_{ox} enhancements in TiO_2 and ATO were identical to three-fold, which coincided with the dielectric constant enhancement of three-fold between MoO_2 and TiN (Fig. 4e), indicating that t_{ox} scaling achieved by developing the MoO_2 electrode was attributed to the contributions of the high dielectric constant of TiO_2. Additionally, according to the leakage-current density *versus* voltage (*J*–*V*) curves (Fig. S6b, ESI†), the leakage current of the MIM capacitor fabricated using the MoO_2 electrode was reduced by approximately 1–2 orders of magnitude compared to the capacitor fabricated using the TiN electrode. Because leakage current was predominantly conducted by the Schottky emission

View Article Online

Published on 08 August 2022. Downloaded on 9/30/2022 7:42:00 AM.

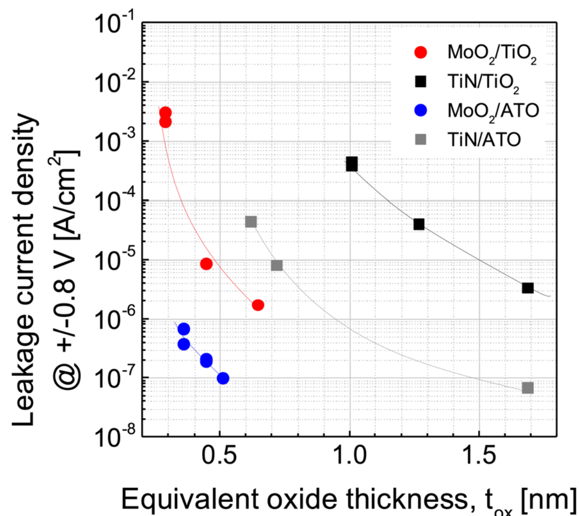

Fig. 6 J–t_{ox} plots for TiO_2 and ATO thin films deposited on MoO_2 and TiN substrates. The lines serve as a guide to the eye for the trend in the J–t_{ox} plots.

mechanism in TiO_2, the barrier height between the electrode and insulator markedly affected the leakage current. The MoO_2 work function is approximately 1 eV higher than the TiN one, thereby effectively reducing the MIM capacitor leakage current in the TiO_2-based insulator. In the case of ATO, significant Schottky emission mediated leakage current reduction was observed. The Schottky emission along with overcoming the Schottky barrier resulted in the Schottky emission induced leakage current conduction in TiO_2, where the applied voltage was sufficient to overcome the barrier (generally 0.5–1.0 V).[41,42] In the case of the MoO_2 electrode, the leakage current reduction was dramatically decreased compared to that of the TiN electrode for the applied voltage above ±0.5 V (Fig. S6b, ESI†). Therefore, the decrease in leakage current with the use of the MoO_2 electrode can be attributed to the higher work function of MoO_2. Although t_{ox} scaling has only been attempted using conventional high-k materials, such materials exhibit a tradeoff relationship between the dielectric constant and the bandgap, which inherently limits t_{ox} scaling. Therefore, using MoO_2 films can scale t_{ox} by simultaneously enhancing the dielectric constant and leakage current.

Conclusions

An ALD process was developed to deposit MoO_2 thin films for application to DRAM capacitor electrodes, and the electrical characteristics of MIM capacitors fabricated using the MoO_2 thin films were evaluated. The MoO_2 films deposited using O_3 on the TiN substrate were highly crystallized. The metastable-phase formation mechanism revealed that the rutile-TiO_2-induced template effect on the TiN surface contributed to the high MoO_2 crystallinity, which induced a rutile microstructure in the TiO_2 deposited on the MoO_2 layer. This feature resulted in a dielectric constant as high as 150, the highest ever reported for deposited TiO_2 thin films. Moreover, the very high MoO_2 work function of 5.5 eV effectively suppressed the leakage current, enabling the MIM capacitor to achieve a t_{ox} scaling of 0.357 nm. Consequently, the developed MoO_2 ALD method could substantially enhance the electrical properties of next-generation DRAM devices.

Author contributions

The manuscript was written through contributions of all authors. All authors have given approval to the final version of the manuscript. Y. W. Kim, A. J. Lee, D. H. Han, and D. C. Lee performed thin film deposition, device fabrication, and characterization. J. H. Hwang and Y. Kim carried out device fabrication. S. Moon and T. Youn performed chemical analyses. M. Lee and W. Jeon designed the experiment and co-wrote the paper. All of the authors discussed the results and commented on the paper.

Conflicts of interest

There are no conflicts to declare.

Acknowledgements

This work was supported by the Technology Innovation Program (No. 20017216). W. Jeon also acknowledges financial support by SK Hynix Inc.

Notes and references

1 W. Jeon, *J. Mater. Res.*, 2020, **35**, 775–794.
2 S. K. Kim and M. Popovici, *MRS Bull.*, 2018, **43**, 334–339.
3 E. Y. Jung, J. Bang, J. H. Hwang, D. H. Han, Y. Kim, H. Kim and W. Jeon, *Nanotechnology*, 2021, **32**, 045201.
4 W. Jeon, Y. Kim, C. H. An, C. S. Hwang, P. Gonon and C. Vallee, *IEEE Trans. Electron Devices*, 2018, **65**, 660–666.
5 D. S. Kwon, C. H. An, S. H. Kim, D. G. Kim, J. Lim, W. Jeon and C. S. Hwang, *J. Mater. Chem. C*, 2020, **8**, 6993–7004.
6 F. Chiu, *Adv. Mater. Sci. Eng.*, 2014, **2014**, 1–18.
7 C. H. An, W. Lee, S. H. Kim, C. J. Cho, D.-G. Kim, D. S. Kwon, S. T. Cho, S. H. Cha, J. il Lim, W. Jeon and C. S. Hwang, *Phys. Status Solidi RRL*, 2019, **13**, 1800454.
8 N. Menou, M. Popovici, K. Opsomer, B. Kaczer, M. A. Pawlak, C. Adelmann, A. Franquet, P. Favia, H. Bender, C. Detavernier, S. Van Elshocht, D. J. Wouters, S. Biesemans and J. A. Kittl, *Jpn. J. Appl. Phys.*, 2010, **49**, 04DD01.
9 T. F. Nova, A. S. Disa, M. Fechner and A. Cavalleri, *Science (1979)*, 2019, **364**, 1075–1079.
10 M. Popovici, B. Kaczer, V. V. Afanas'ev, G. Sereni, L. Larcher, A. Redolfi, S. Van Elshocht and M. Jurczak, *Phys. Status Solidi RRL*, 2016, **10**, 420–425.
11 W. Lee, C. H. An, S. Yoo, W. Jeon, M. J. Chung, S. H. Kim and C. S. Hwang, *Phys. Status Solidi RRL*, 2018, **12**, 1–6.

This journal is © The Royal Society of Chemistry 2022

12 W. Weinreich, L. Wilde, J. Müller, J. Sundqvist, E. Erben, J. Heitmann, M. Lemberger and A. J. Bauer, *J. Vac. Sci. Technol., A*, 2013, **31**, 01A119.
13 S. Zarubin, E. Suvorova, M. Spiridonov, D. Negrov, A. Chernikova, A. Markeev and A. Zenkevich, *Appl. Phys. Lett.*, 2016, **109**, 0–5.
14 J. Kim, B. S. Kim, A. J. Lee, D. H. Han, J. H. Hwang, Y. Kim, K. C. Song, H. Oh, S. Kim, Y. Park and W. Jeon, *Ceram. Int.*, 2021, **48**, 3236–3242.
15 L. P. B. Lima, J. A. Diniz, I. Doi and J. Godoy Fo, *Microelectron. Eng.*, 2012, **92**, 86–90.
16 M. Rose, J. Niinistö, P. Michalowski, L. Gerlich, L. Wilde, I. Endler and J. W. Bartha, *J. Phys. Chem. C*, 2009, **113**, 21825–21830.
17 N. Menou, X. P. Wang, B. Kaczer, W. Polspoel, M. Popovici, K. Opsomer, M. A. Pawlak, W. Knaepen, C. Detavernier, T. Blomberg, D. Pierreux, J. Swerts, J. W. Maes, P. Favia, H. Bender, B. Brijs, W. Vandervorst, S. van Elshocht, D. J. Wouters, S. Biesemans and J. A. Kittl, *Tech. Dig. - Int. Electron Devices Meet.*, 2008, 1–4.
18 W. Lee, C. J. Cho, W. C. Lee, C. S. Hwang, R. P. H. Chang and S. K. Kim, *J. Mater. Chem. C*, 2018, **6**, 13250–13256.
19 X. Rui, P. Kumar, H. Chen and S. Malhotra, *US Pat.*, 8415657, 2013, Intermolecular, Inc.
20 M. F. J. Vos, B. Macco, N. F. W. Thissen, A. A. Bol and W. M. M. (Erwin) Kessels, *J. Vac. Sci. Technol., A*, 2016, **34**, 01A103.
21 J. N. Kvalvik, J. Borgersen, P.-A. Hansen and O. Nilsen, *J. Vac. Sci. Technol., A*, 2020, **38**, 042406.
22 M. Diskus, O. Nilsen and H. Fjellvåg, *J. Mater. Chem.*, 2011, **21**, 705–710.
23 Y. Cho, S. H. Kim, B. S. Kim, Y. Kim and W. Jeon, *Phys. Chem. Chem. Phys.*, 2021, **23**, 2568–2574.
24 J. Yang, S. Kim, W. Choi, S. H. Park, Y. Jung, M.-H. Cho and H. Kim, *ACS Appl. Mater. Interfaces*, 2013, **5**, 4739–4744.
25 M. Mattinen, P. J. King, L. Khriachtchev, M. J. Heikkilä, B. Fleming, S. Rushworth, K. Mizohata, K. Meinander, J. Räisänen, M. Ritala and M. Leskelä, *Mater. Today Chem.*, 2018, **9**, 17–27.
26 J. D. DeLoach and C. R. Aita, *J. Vac. Sci. Technol., A*, 1998, **16**, 1963–1968.
27 Y. S. Kang, C. Y. Kim, M. H. Cho, K. B. Chung, C. H. An, H. Kim, H. J. Lee, C. S. Kim and T. G. Lee, *Appl. Phys. Lett.*, 2010, **97**, 2008–2011.
28 H. K. Kim, S. Y. Lee, I. Yu, T. J. Park, R. Choi and C. S. Hwang, *IEEE Electron Device Lett.*, 2012, **33**, 955–957.
29 S. K. Kim, G. W. Hwang, W. D. Kim and C. S. Hwang, *Electrochem. Solid-State Lett.*, 2006, **9**, 2005–2007.
30 J. H. Han, S. Han, W. Lee, S. W. Lee, S. K. Kim, J. Gatineau, C. Dussarrat and C. S. Hwang, *Appl. Phys. Lett.*, 2011, **99**, 2009–2012.
31 M. Schuisky, J. Aarik, K. Kukli, A. Aidla and A. Hårsta, *Langmuir*, 2001, **17**, 5508–5512.
32 K. Fröhlich, J. Aarik, M. Ťapajna, A. Rosová, A. Aidla, E. Dobročka and K. Hušková, *J. Vac. Sci. Technol., B: Microelectron. Nanometer Struct.*, 2009, **27**, 266.
33 Y. Yan, D. Zhou, C. Guo, J. Xu, X. Yang, H. Liang, F. Zhou, S. Chu and X. Liu, *J. Sol-Gel Sci. Technol.*, 2016, **77**, 430–436.
34 W. Jeon, S. Yoo, H. K. Kim, W. Lee, C. H. An, M. J. Chung, C. J. Cho, S. K. Kim and C. S. Hwang, *ACS Appl. Mater. Interfaces*, 2014, **6**, 21632–21637.
35 S. W. Lee, J. H. Han, S. Han, W. Lee, J. H. Jang, M. Seo, S. K. Kim, C. Dussarrat, J. Gatineau, Y.-S. Min and C. S. Hwang, *Chem. Mater.*, 2011, **23**, 2227–2236.
36 H. Shima, F. Takano, H. Muramatsu, H. Akinaga, I. H. Inoue and H. Takagi, *Appl. Phys. Lett.*, 2008, **93**, 113504.
37 S. Lee, B. A. Apgar and L. W. Martin, *Adv. Energy Mater.*, 2013, **3**, 1084–1090.
38 S. Kupke, S. Knebel, U. Schroeder, S. Schmelzer, U. Bottger and T. Mikolajick, *IEEE Electron Device Lett.*, 2012, **33**, 1699–1701.
39 W. Jeon, H.-S. Chung, D. Joo and S.-W. Kang, *Electrochem. Solid-State Lett.*, 2008, **11**, H19.
40 M. Pešić, S. Knebel, M. Geyer, S. Schmelzer, U. Böttger, N. Kolomiiets, V. V. Afanas'ev, K. Cho, C. Jung, J. Chang, H. Lim, T. Mikolajick and U. Schroeder, *J. Appl. Phys.*, 2016, **119**, 064101.
41 W. Jeon, S. H. Rha, W. Lee, Y. W. Yoo, C. H. An, K. H. Jung, S. K. Kim and C. S. Hwang, *ACS Appl. Mater. Interfaces*, 2014, **6**, 7910–7917.
42 W. Jeon, S. H. Rha, W. Lee, C. H. An, M. J. Chung, S. H. Kim, C. J. Cho, S. K. Kim and C. S. Hwang, *Phys. Status Solidi RRL*, 2015, **9**, 410–413.

Published on 08 August 2022. Downloaded on 9/30/2022 7:42:00 AM.